


Quantum Sensing of Magnetic Fields Using Global Optimization Algorithms

Wei Xiao¹, Yudong Ding, Teng Wu^{1,*}, Xiang Peng¹, and Hong Guo^{1,†}

State Key Laboratory of Advanced Optical Communication Systems and Networks, School of Electronics, and Center for Quantum Information Technology, Peking University, Beijing 100871, China

 (Received 13 February 2023; revised 16 July 2023; accepted 25 July 2023; published 17 August 2023)

Experimentally achieving optimal performance of quantum sensors, such as optically pumped magnetometers, is usually challenging and time consuming due to the complexity of the physical system. For a given experiment scheme, there are usually many experiment parameters that need to be fine tuned for achieving a satisfying performance of the quantum sensor. By employing global optimization algorithms, we propose an automatic and efficient way to optimize the sensor performance. We take the most sensitive magnetic field sensor, i.e., the optically pumped magnetometer, as an example to demonstrate how these algorithms facilitate the automatic optimization of quantum sensors. Both the optimization of zero-field magnetometers in a magnetic shield and the finite-field magnetometers in open Earth's field are demonstrated. A noise floor of approximately $10 \text{ fT/Hz}^{1/2}$ is achieved within a short time. This method provides an efficient way for quantum sensor optimization and will be helpful for the quantum sensor design.

DOI: [10.1103/PhysRevApplied.20.024042](https://doi.org/10.1103/PhysRevApplied.20.024042)

I. INTRODUCTION

Quantum sensing plays a fundamental role in physics, as it constitutes a key ingredient of many state-of-the-art applications and experiments. As a common physical quantity that is all around the world, magnetic field sensing has been applied in various fields, such as high-precision fundamental measurements [1–3], detection of magnetic anomaly signals [4–6], detection of nuclear magnetic resonance signals [7–10], and biomagnetic field measurements [11–14]. The optically pumped magnetometer (OPM) is one of the most sensitive sensors for measuring magnetic fields and achieves a sensitivity of $\text{sub-fT/Hz}^{1/2}$ [15–17], which is comparable or even surpassing to superconducting quantum interference devices (SQUIDS).

To achieve a better performance of the OPM, the whole system of the OPM is usually complex and made up of many significant components that determine the performance, such as the laser light, the atomic vapor cell, the modulation magnetic fields, and the auxiliary circuits. Traditionally, all the experiment parameters are tuned by researchers based on theoretical guidance and their experience. Such a manual optimization procedure is usually challenging, time consuming and even results in different performances for different people. For example, an experienced researcher can usually achieve a better performance than a novice researcher can achieve.

By regarding the performance optimization as a global optimization problem in mathematics that attempts to find the global minima or maxima of an objective function (the performance) on a given set of parameters, we can optimize the performance automatically under the guidance of algorithms. Whether the derivative of the objective function is known or not, the optimization algorithm can be simply categorized into two main categories, i.e., the derivative-based algorithm and the derivative-free algorithm. For practical physical systems, an exact expression for the dependence of the performance on parameters is usually unavailable, and thus we cannot extract the derivative information directly. To address this issue, we can approximate the derivative by repeatedly evaluating the objective function after introducing small perturbations to the parameters along each dimension. Although it is possible to utilize derivative-based algorithms even without an exact derivative expression, this approach is generally not very efficient due to the number of function evaluations required to approximate the derivative, which increases with the dimensions of the problem, and have the risk of leading to local optima. So, we mainly focus on the derivative-free optimizations (or called black-box optimizations) to deal with a practical system.

Many algorithms have been proposed and tested to find the globally best parameters, such as Bayesian optimization (BO) [18], particle swarm optimization (PSO) [19], evolution strategy [20], simulated annealing [21], etc. The derivative-free algorithms have been used in many fields, such as the multiple-parameter optimization of laser cooling and Bose-Einstein condensation [22–25],

*wuteng@pku.edu.cn

†hongguo@pku.edu.cn

quantum optimal control [26–29] in quantum physics [30, 31], materials design, and synthesis [32–34] in materials science [35,36], etc. With the algorithms, the sensors can be optimized automatically without requiring any human intervention. In this way, much time can be saved to design a better experimental protocol instead of being wasted on time consuming and repetitive optimization work. Furthermore, such a method can be useful for sensors that require long-term continuous operation, such as searching for exotic physics [6,37,38] and monitoring the geomagnetic field [39]. If something unexpected happens and the sensor does not work properly, this method can automatically rediscover the best working status to ensure the sensor always has the best working performance without manual maintenance.

In this paper, we propose and demonstrate an automatic optimization method based on derivative-free algorithms to optimize the OPMs. To fully demonstrate the feasibility and high efficiency of the automatic optimization method, we experimentally implement the method in two kinds of OPMs. We have optimized the spin-exchange relaxation-free (SERF) OPM in a zero-field environment and the magnetic resonance-based OPM in open Earth’s field. Both of the OPMs can be optimized to their optimal performances, 10 fT/Hz^{1/2} for SERF OPMs and 20 fT/Hz^{1/2} for magnetic resonance-based OPMs. The optimization procedure takes only several minutes to about tens of minutes, which depends on the number of parameters to be optimized. The Bayesian optimization (BO), particle swarm optimization (PSO), and differential evolution (DE) algorithms have been implemented and discussed.

II. OPTIMIZATION ALGORITHM DESIGN

The optimization algorithms attempt to find a set of parameters (x_1, \dots, x_N) to maximize or minimize an objective function $f(x_1, \dots, x_N)$ in parameter spaces, where N indicates the number of parameters to be optimized. To apply the algorithms in the performance optimization of OPMs, we first need to define an objective function that describes the performances. Since the sensitivity is usually the most significant specification of OPMs, the sensitivity is taken as an example to demonstrate the implementation of the algorithms in this paper.

The magnetic field noise amplitude spectral density (ASD) is a commonly used indicator to evaluate the sensitivity of OPMs. To make sure the OPM can measure magnetic fields normally during the optimization process, we actively apply a calibration field to the OPM by magnetic field coils and take the SNR as the objective function that describes the performance of OPMs. Figures 1(b) and 1(c) show the measured magnetic field signal in the time domain and frequency domain, respectively. By applying a sinusoidal calibration field with an amplitude of 10 pT and a frequency of 75 Hz, there will be a spike at 75 Hz

in the ASD of the OPM. The SNR is defined as the ratio between the spike amplitude and the noise floor around the spike. Obviously, a higher SNR indicates a higher sensitivity of OPMs. With the objective function defined, various algorithms have been proposed to deal with such optimization problems. Furthermore, we have to note that there must exist noise for the objective function of a real experiment system. For the same parameters, the value of the objective function is not a constant but a variable with a specific distribution. By conducting 500 measurements of the SNR using the same optimal parameters, as depicted in Fig. 1(d), we observed a relative fluctuation of approximately 10% in the SNR. This variation could be attributed to the random noise in the OPM and the algorithm utilized for estimating the amplitude spectral density. So, the global optimization algorithms should be noise robust. Although, measuring sensitivities over a longer data-recording time would reduce the uncertainty in the sensitivity, it would might slow down the algorithm and increase the time required to complete the optimization process. Considering the uncertainty in the sensitivity, to report the ultimate sensitivity more accurately, we can save several sets of parameters that approach the highest sensitivity during the process, measure their corresponding sensitivities in a longer data-recording time and take the highest sensitivity as the ultimate sensitivity.

For the SNR of OPMs, three typical and different kinds of algorithms are selected to optimize the OPM, i.e., the PSO, BO, and DE algorithms. Both the PSO and DE are metaheuristic optimization methods inspired by biological and sociological motivations, and usually make few or no assumptions about the problem being optimized. PSO works similarly to a swarm of birds searching for a food source (the optimal performance) while DE optimizes a problem by iteratively improving a candidate solution based on an evolutionary process. Unlike stochastic algorithms such as DE and PSO, BO relies on building a probabilistic surrogate model for approximating the objective function from accumulated observations and uses an acquisition function defined from this surrogate to decide where to sample the parameter space. For BO using the Gaussian process, it typically assumes that the optimization parameters are independent. Although these algorithms are different in detailed optimization processes, they have similar procedures to optimize the performance. In step 1, we first randomly select some set of parameters as initial parameters to test the performance of OPM. Step 2, finding the next set of parameters that are expected to obtain a better performance based on the algorithm. Step 3, testing the performance with parameters in step 2 and determining whether the termination criterion is satisfied. If so, the optimization procedure is finished. Otherwise, step 2 is repeated again until the termination criterion is satisfied, such as the performance is converging or achieves a satisfying value.

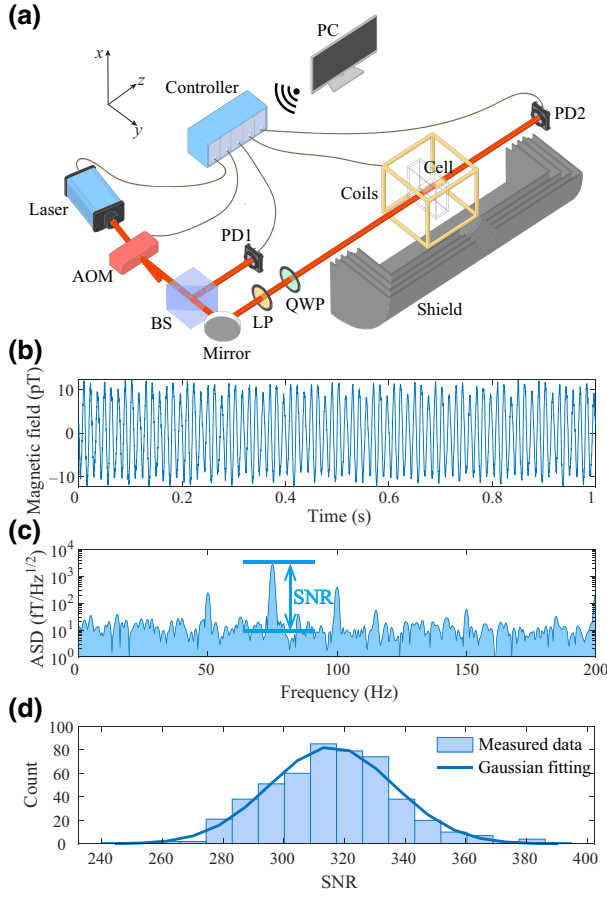


FIG. 1. (a) Schematic of the single-beam zero-field OPM. A circularly polarized light propagating along the z axis is performed as optical pumping and probing the atoms confined in an atomic vapor cell. To achieve higher sensitivity, the light power is actively stabilized with an acoustic-optical modulator (AOM). All the electronic devices are connected to the controller for remote operations on the computer. BS, beam splitter; LP, linear polarizer; QWP, quarter-wave plate; PD, photodiode. (b) The output of the OPM when applying a sinusoidal calibration field with an amplitude of 10 pT and a frequency of 75 Hz. (c) The ASD of the OPM output when applying the calibration field. The ratio between the spike amplitude of the calibration field and the noise floor around the spike is defined as the SNR that aims to be optimized. To estimate the noise floor, we consider a frequency range of 60 to 90 Hz to avoid power-line interference. Additionally, we exclude the frequency range of 73 to 77 Hz to eliminate any interference caused by the calibration field. The noise floor is estimated to be the average of the ASD within the specified frequency range. (d) The histogram of the SNR for 500 times measurement with the same parameters. If fitting the result with the Gaussian function, we obtain a standard deviation of $\sigma = 29$. A longer data-recording time would reduce the uncertainty in SNR measurements, but at the cost of prolonging each step of the optimization process.

III. RESULTS

According to the dynamic range of OPM, it can be divided into two categories, the zero-field OPM and the

finite-field OPM. To comprehensively demonstrate the application of the algorithm in OPM performance optimizations, both the two kinds of OPMs are tested and an optimal performance is achieved.

A. OPM IN ZERO FIELD

The zero-field OPM, which is operated in zero or near-zero fields, is usually based on the level-crossing resonance [40]. As one of the most sensitive magnetic field sensors, the zero-field OPM based on the SERF mechanism can achieve a sensitivity of sub-fT/Hz^{1/2} with a well-designed experiment system [15]. Due to the advantages of high sensitivity, low cost, and small size [41,42], the SERF OPM has gained a lot of attention recently, especially in the community of biomagnetic measurement [11,12,43–45].

In this paper, we demonstrate a zero-field OPM with a compact single-beam architecture, which is a popular scheme for practical applications. The schematic of the OPM is shown in Fig. 1(a). The light emitted by a 795-nm distributed Bragg reflector (DBR) laser is sent through a linear polarizer (LP) and a quarter-wave plate (QWP) to produce a circularly polarized light. The light is performed as the pump light to polarize atoms confined in the atomic vapor cell and detect the atomic spin polarization. To reduce the intensity noise of the light, we actively stabilize the laser power with an acousto-optic modulator (AOM). A part of the first-order diffracted beam is reflected by a beam splitter (BS) and picked up by a photodiode (PD) for power stabilizations. A $6 \times 6 \times 3$ mm³ cell, filled with ⁸⁷Rb and 600 Torr N₂, is heated to 150 °C and placed inside a cylindrical magnetic shield. The Helmholtz coils inside the shield generate a parametric modulation field $B_1 \cos \omega t$ along x direction. Under such a transverse parametric modulation, the atomic spin polarization along z direction is

$$P_z(\omega_z) = 2P_0 J_0(\eta) J_1(\eta) \frac{\Gamma \gamma B_{0x}}{\Gamma^2 + \gamma^2 B_{0x}^2} \sin \omega t, \quad (1)$$

where Γ is the total relaxation rate, P_0 is the equilibrium spin polarization in the absence of magnetic fields, J_n is the Bessel function of order n , $\eta = \gamma B_1 / \omega$ is the modulation index, γ is the gyromagnetic ratio, and B_{0x} is the x -axis magnetic field to be measured. As the absorption of the light depends on the polarization along the z axis, which is a form of dispersive Lorentzian curve centered around $B_{0x} = 0$ as indicated in Eq. (1), the magnetic fields can be extracted by demodulating the PD2 signal with a lock-in amplifier.

The sensitivity of this kind of absorption-based OPM is often limited by the light intensity noise [46], so the PD1 signal is taken as the reference signal to feedback control the light power through the AOM, where a proportion integration differentiation (PID) module is employed as the

feedback controller. A well-stabilized light power usually indicates a higher sensitivity limit of the OPM. For the experiment scheme shown in Fig. 1(a), the sensitivity of the OPM is determined by many factors, such as the light frequency f_{light} , the light power P_{light} , the modulation field amplitude B_1 and frequency ω , and PID parameters (K_P , K_I , K_D). In this case, we can denote the OPM sensitivity \mathcal{S} as

$$\mathcal{S} = \mathcal{S}(f_{\text{light}}, P_{\text{light}}, B_1, \omega, K_P, K_I, K_D), \quad (2)$$

which indicates the sensitivity \mathcal{S} is a function of these seven parameters. By employing algorithms to find a set of optimal parameters, an optimal sensitivity can be achieved automatically.

The optimization process of the OPM sensitivity is depicted in Fig. 2, where dots are sensitivities under different test parameters generated by the algorithms, and the line represents the moving best sensitivity of these dots. Given such an OPM setup, the optimal sensitivity that can be achieved is about $10 \text{ fT/Hz}^{1/2}$ limited by technical noise. For the 250 iterations shown in Fig. 2, all the three algorithms can obtain several sets of parameters achieving the optimal sensitivity. Each iteration takes about 0.7 s, of which 0.5 s is used to record the output of the OPM and 0.2 s is used to find the next set of parameters expected to have a better performance and communicate with these electronic instruments. The whole optimization process only takes about 3 min, which is not only much faster but also automatic. Certainly, different algorithms show different optimization processes. The PSO converges quickly towards the best parameters compared with the other two algorithms. We note that even after 250 iterations the DE and BO algorithms were still exploring the parameter space in an attempt to achieve better performance (as evidenced by the variety of sensitivities on the right-hand side of the plot). Although the DE and BO algorithms are not converged after 250 iterations, they are still useful in practical applications since they can also find the parameters achieving the best sensitivity. The experiment has been repeated and tested many times using randomly selected initial parameters and shows similar results as depicted in Fig. 2.

B. OPM in geomagnetic field

Compared with the zero-field OPM that usually operates in a magnetically shielded device for shielding the external environment, the finite-field OPM has a larger dynamic range and can work directly in the open geomagnetic field. The better applicability makes it ideal for use in a wide range of existing and emerging applications, such as unshielded biomagnetic measurements [13,47] and geophysical explorations [48,49]. A Bell-Bloom magnetometer [50–53] is developed and it achieves a sensitivity

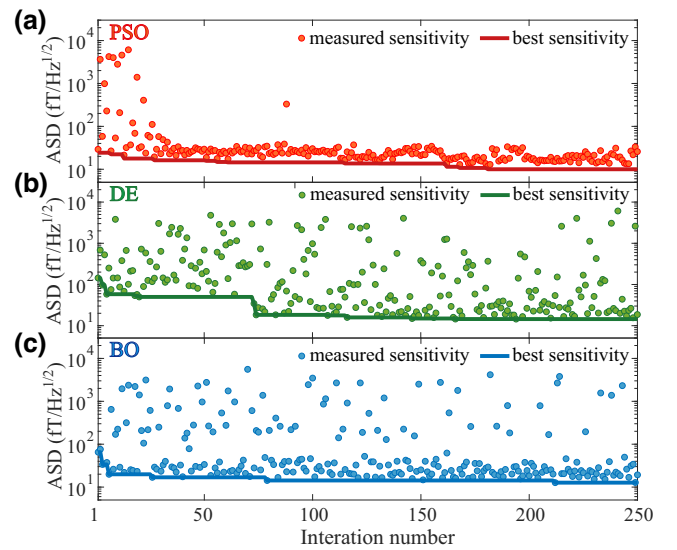


FIG. 2. Optimization results of the zero-field OPM based on PSO (a), DE (b), and BO (c) algorithms. Each dot in the plot represents a specific set of tested experiment parameters, and the line depicts the moving highest sensitivity during the optimization process.

of $20 \text{ fT/Hz}^{1/2}$ in the open environment with the help of the algorithms.

The magnetometer is based on a pump-probe scheme to polarize the atomic cesium spins and monitor the Larmor precession. As shown in Fig. 3(a), a circularly polarized pump beam is used to align the atomic spins along its transmission direction. The light intensity is modulated on and off at the Larmor frequency, which is proportional to the magnetic field strength. In this case, the spins aligned at different times coherently add together and form a macroscopic magnetic moment precessing at the Larmor frequency. The vapor cell is antirelaxation coated and is kept at room temperature, with a typical magnetic resonance linewidth of approximately 5 Hz. The output signal from the balanced photodetector is demodulated with a lock-in amplifier to extract magnetic field information.

Due to the operation of the OPM in an unshielded and noisy geomagnetic field, it is necessary to employ a closed-loop mode to extend its dynamic measurement range. This can be achieved by either adjusting the modulation frequency of the pump light to track the changing Larmor frequency [54–56] or compensating for magnetic field drifts to stabilize the bias field [57–60]. In our experimental setup, we implement a closed-loop system by utilizing feedback control to adjust the modulation frequency of the pump light. This approach enables us to directly extract the measured magnetic field value from the modulation frequency, thereby maintaining stability and accuracy in the presence of field fluctuations and noise. By employing this closed-loop configuration, we enhance the performance

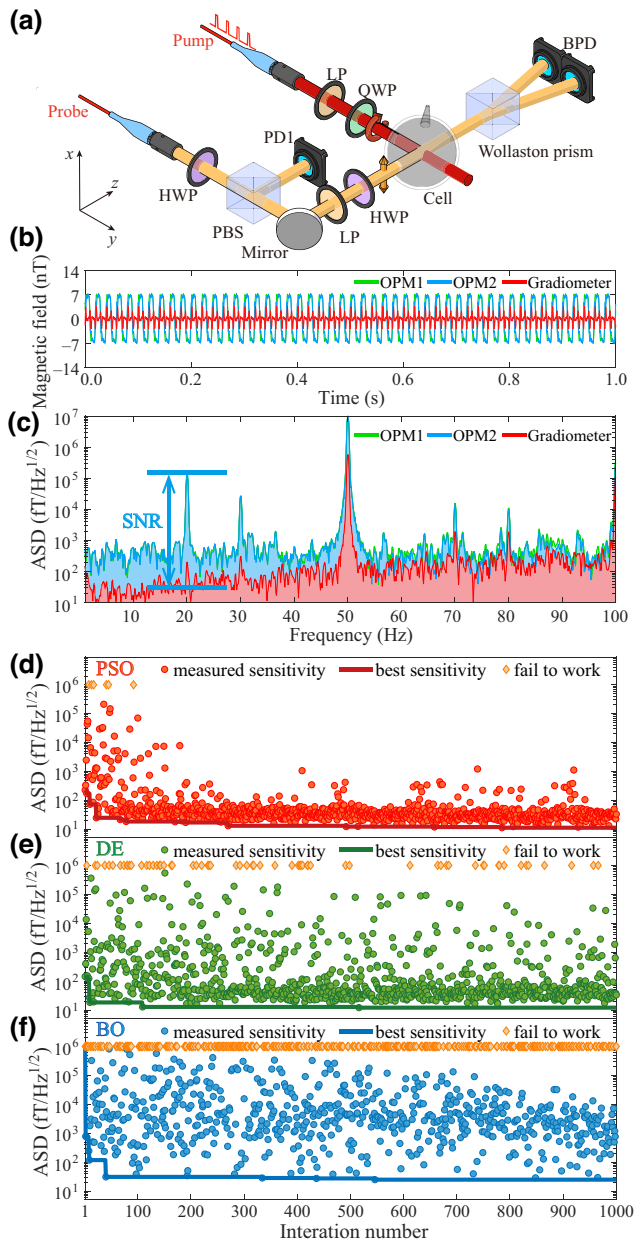


FIG. 3. (a) Schematic of the finite-field OPM. An amplitude-modulated circularly polarized light propagating along the y axis is performed as optical pumping. The Larmor precession of atomic spins is detected with a linearly polarized light via optical rotation. BPD, balanced photodiode. (b) The output of the OPMs in an opening environment. A strong power-line interference, up to approximately 14 nT, caused by a high-voltage line nearby can be observed. (c) The ASD of the OPM when applying a calibration field with an amplitude of 10 pT and a frequency of 20 Hz. The ratio between the spike amplitude of the OPMs and the noise floor of the differential measurements around the spike is defined as the SNR. Optimization results of finite-field OPMs based on PSO (d), DE (e), and BO (f) algorithms show that OPMs can also be optimized in an unshielded challenging environment. The orange diamond corresponds to one set of parameters that the OPMs fail to work.

of OPM and enable reliable measurements within the challenging unshielded geomagnetic field environment.

Furthermore, the magnetic field noise from surroundings would deteriorate OPM performances [61], and there are some algorithm-driven methods have been proposed to address this problem [62,63]. Figure 3(b) shows the measured magnetic field of surroundings by OPMs, and a strong power-line interference, up to approximately 14 nT, caused by a high-voltage line nearby can be observed. To achieve a high sensitivity in such a challenging environment, two OPMs depicted in Fig. 3(a) are built to perform differential (gradiometric) measurements. One OPM serves as a reference OPM monitoring the background magnetic field noise, while another OPM serves as the measurement OPM for measuring the magnetic field of interest. In this case, the background magnetic field noise can be suppressed by subtracting the output of the reference OPM from the output of the measurement OPM. The two OPMs must feature a good consistency to effectively suppress the background magnetic field noise. To actually characterize the performance of OPMs, the SNR is defined as the ratio between the spike amplitude of the OPM (induced by the calibration field) and the noise floor of the OPMs operated in the gradiometric mode around the spike, as shown in Fig. 3(c). The signal amplitude of the OPM ensures that the OPM is still sensitive to the magnetic field, while the noise floor of the differential measurements indicates the intrinsic sensitivity of the OPMs. The frequency range used to estimate the noise floor is set to be 12 to 28 Hz, excluding the range of 18 to 22 Hz. In this case, if the OPMs are not configured correctly and experience failure or poor performance as a result, the resulting SNR would approach zero. The modulation frequency of the calibration field is set to 20 Hz to avoid interference from the background noise.

The sensitivity of the OPM is determined by many parameters. For example, the frequency of the pump light determines the population of the two ground-state hyperfine levels, the frequency of the probe light determines the detected signal amplitude and which hyperfine level to be detected, the power of the pump light determines the spin polarization, etc. Furthermore, the closed-loop configuration of OPM can increase the bandwidth due to the limited spin relaxation rate [55,64]. A high bandwidth usually results in a high common-mode rejection ratio (CMRR) of surrounding noise [13,65]. So, the PID parameters are also significant to the gradiometer performance. All together 15 experiment parameters need to be optimized. For such a complex experiment system, it usually takes days or even weeks to manually optimize it. Sometimes it may not be optimized to its best performance without the guidance of experienced researchers.

Figures 3(d)–3(f) show the optimization results of the three algorithms. Since there are more parameters to be

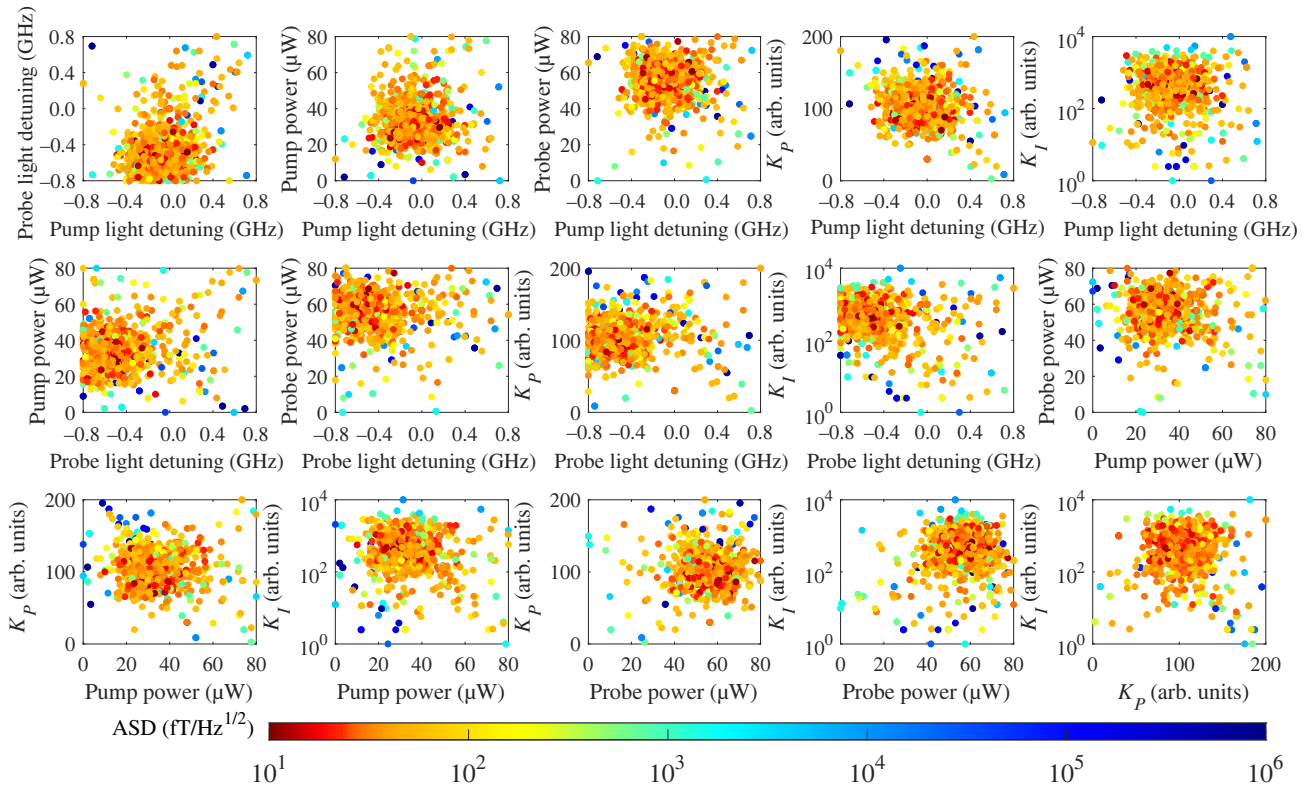


FIG. 4. Searching the parameter space with the PSO algorithm, where every dot represents one set of tested parameters. For simplicity of visualization, we demonstrate only the parameter space related to OPM1. The pump light detuning is defined as the frequency difference between the pump light frequency and the D1 transition line (from $6^2S_{1/2} F = 3$ to $6^2P_{1/2} F' = 4$) of cesium atoms. The probe light detuning is defined as the frequency difference between the probe light frequency and the D2 transition line (from $6^2S_{1/2} F = 4$ to $6^2P_{3/2} F' = 5$) of cesium atoms.

optimized, which indicates a larger parameter space to be explored, more iterations are needed to find a set of optimal parameters. For the 1000 iterations, the results of PSO converges quickly toward the optimal parameters that achieve a sensitivity of 20 fT/Hz^{1/2}, which is also the best sensitivity we have obtained before in the same setup [13]. As there are several PID loops employed in the OPMs, the OPMs may fail to work for some tested parameters. For example, when the PID parameters are not suitable, the PID output would oscillate around the setpoint. If the amplitude of the oscillations increases with time, the system is unstable. In this case, the OPM is insensitive to the magnetic field and its output signal is meaningless. These unsuitable parameters are marked with orange diamonds in Fig. 3(d).

The DE algorithm shows a similar result depicted in Fig. 2(b). Although the obtained sensitivities appear to converge and several sets of optimal parameters have been situated, the algorithm still explore the parameter space even after 1000 iterations. For the BO algorithm, it explores the entire parameter space all the time without converging. The reason for the failure of the BO algorithm may be attributed to several factors, such as the general BO

algorithm itself is more suitable for low-dimension optimization problems rather than high-dimension problems [18], and these experiment parameters are inter-related, which would break the independent parameters assumption of the BO algorithm.

Figure 4 shows the process of exploring the parameter space based on the PSO algorithm, where each dot on the plot corresponds to one set of tested parameters. To give a clear visual representation, we have included a series of two-dimensional diagrams to depict the process. For simplicity, only some parameters related to OPM1 are demonstrated. Otherwise, there will be $(15 \times 14)/2 = 105$ subfigures to be plotted for such a high-dimension optimization problem. As shown in Fig. 4, the algorithm randomly searches the entire parameter space for optimal parameters at the beginning of the optimization process. However, as the number of iterations increases, the algorithm develops a deeper understanding of the OPM system. Consequently, the search space will gradually approach and finally converge to the region where the optimal parameters are situated.

Since the objective function is affected by noise, its value will fluctuate for every measurement. So, the

algorithm eventually converges towards an optimal region in the parameter space rather than a specific point, as shown in Fig. 4.

For a global optimization problem, the algorithm may get stuck in a local optimum without finding a global optimum. One way to solve such a problem is the noise strategy [66], which involves actively introducing random noise when searching for the next set of parameters. For real physical systems like the OPMs, the noise strategy is naturally implemented due to the fluctuations of the SNR. We have conducted multiple optimization experiments with different initial parameters, and the results are consistent. Moreover, the results shown in Fig. 4 imply that there is only one optimal region for achieving the optimal sensitivity, which indicates that the optimization problem of the OPM is unimodal for the specified parameter space.

To ensure sufficient frequency resolution of the ASD, a longer data recording time is needed in finite-field OPMs because the calibration field frequency used is lower than in zero-field OPMs. Every iteration takes about 1.2 s, of which 1 s is used to record the output of OPMs and 0.2 s is used to find the next set of parameters and communicate with the instruments. All the optimization process takes only about 20 min, which is much faster and more effective compared with manual operations. As shown in Fig. 3(c), with the help of optimization algorithms, we successfully realize a high-performance gradiometer, which features a high sensitivity of $20 \text{ fT/Hz}^{1/2}$ and a high CMRR of approximately 1000 at 20 Hz.

IV. CONCLUSION

In conclusion, we have taken the magnetometer as an example to demonstrate the application of optimization algorithms in the performance optimization of quantum sensors. Based on the algorithms, the OPM is automatically optimized to its best sensitivity in a short time (typically a few minutes to a dozen minutes), without making any prior assumptions.

For the zero-field OPM operating in the magnetic shield, seven experiment parameters have been optimized and we have achieved a sensitivity of $10 \text{ fT/Hz}^{1/2}$ within approximately 3 min. For the finite-field OPM operating in the open geomagnetic field, 15 experiment parameters have been optimized and we achieve a sensitivity of $20 \text{ fT/Hz}^{1/2}$ within approximately 20 min. Three different algorithms (PSO, DE, and BO) have been tested in the two kinds of OPMs, and we find the PSO algorithm is more suitable for the OPM optimization in our experiment schemes, which converges more quickly than the other two algorithms. Both of the two kinds of OPMs can be automatically optimized to the best sensitivities that we could achieve manually.

Except for the sensitivity optimization, the bandwidth of the OPM is another significant specification that is

often concerned. The bandwidth can also be optimized through the use of algorithms that employ different objective functions. For example, by applying two calibration fields with different modulation frequencies, the ratio of the response to these two calibration fields can be defined as the objective function for optimization.

Given the wide usage of magnetometers as tools for sensing magnetic fields, the automated optimization of sensor performances proposed in this paper can be useful in many aspects. Whether you are a magnetometer researcher or utilizes it solely as a measuring tool, significant time can be saved to focus on the experiment design rather than the time cost and boring optimization work. Furthermore, for the commercial magnetometer product intended for individuals with limited knowledge about the underlying principle of magnetometers, a built-in optimization algorithm can ensure that the sensor is operated at its best performance wherever the working environment changes.

ACKNOWLEDGMENTS

This work is supported by the National Natural Science Foundation of China (Grants No. 62071012, No. 61571018, No. 61531003, No. 91436210), the National Science Fund for Distinguished Young Scholars of China (Grant No. 61225003), and National Hi-Tech Research and Development (863) Program. T.W. acknowledges the support from the start-up funding for young researchers of Peking University.

-
- [1] M. Pospelov, S. Pustelny, M. P. Ledbetter, D. F. J. Kimball, W. Gawlik, and D. Budker, Detecting Domain Walls of Axionlike Models using Terrestrial Experiments, *Phys. Rev. Lett.* **110**, 021803 (2013).
 - [2] M. S. Safronova, D. Budker, D. DeMille, D. F. J. Kimball, A. Derevianko, and C. W. Clark, Search for new physics with atoms and molecules, *Rev. Mod. Phys.* **90**, 025008 (2018).
 - [3] W. Xiao, M. Liu, T. Wu, X. Peng, and H. Guo, Femtotesla Atomic Magnetometer Employing Diffusion Optical Pumping to Search for Exotic Spin-dependent Interactions, *Phys. Rev. Lett.* **130**, 143201 (2023).
 - [4] S. Pustelny, D. F. Jackson Kimball, C. Pankow, M. P. Ledbetter, P. Włodarczyk, P. Wcisło, M. Pospelov, J. R. Smith, J. Read, W. Gawlik, and D. Budker, The global network of optical magnetometers for exotic physics (gnome): A novel scheme to search for physics beyond the standard model, *Ann. Phys.-Berlin* **525**, 659 (2013).
 - [5] H. Masia-Roig, J. A. Smiga, D. Budker, V. Dumont, Z. Grujić, D. Kim, D. F. Jackson Kimball, V. Lebedev, M. Monroy, S. Pustelny, T. Scholtes, P. C. Segura, Y. K. Semertzidis, Y. C. Shin, J. E. Stalnaker, I. Sulai, A. Weis, and A. Wickensbrock, Analysis method for detecting topological defect dark matter with a global magnetometer network, *Phys. Dark Universe* **28**, 100494 (2020).

- [6] S. Afach, B. C. Buchler, D. Budker, C. Dailey, A. Derevianko, V. Dumont, N. L. Figueroa, I. Gerhardt, Z. D. Grujić, and H. Guo, *et al.*, Search for topological defect dark matter using the global network of optical magnetometers for exotic physics searches (GNOME), *Nat. Phys.* **17**, 1396 (2021).
- [7] I. Savukov and T. Karaulanov, Anatomical MRI with an atomic magnetometer, *J. Magn. Reson.* **231**, 39 (2013).
- [8] G. Bevilacqua, V. Biancalana, Y. Dancheva, A. Vigilante, A. Donati, and C. Rossi, Simultaneous detection of H and D NMR signals in a micro-tesla field, *J. Phys. Chem. Lett.* **8**, 6176 (2017).
- [9] J. W. Blanchard, T. Wu, J. Eills, Y. Hu, and D. Budker, Zero- to ultralow-field nuclear magnetic resonance J-spectroscopy with commercial atomic magnetometers, *J. Magn. Reson.* **314**, 106723 (2020).
- [10] K. Mouloudakis, S. Bodenstedt, M. Azagra, M. W. Mitchell, I. Marco-Rius, and M. C. Tayler, Real-time polarimetry of hyperpolarized ^{13}C nuclear spins using an atomic magnetometer, *J. Phys. Chem. Lett.* **14**, 1192 (2023).
- [11] K. Kim, S. Begus, H. Xia, S.-K. Lee, V. Jazbinsek, Z. Trontelj, and M. V. Romalis, Multi-channel atomic magnetometer for magnetoencephalography: A configuration study, *NeuroImage* **89**, 143 (2014).
- [12] E. Boto, N. Holmes, J. Leggett, G. Roberts, V. Shah, S. S. Meyer, L. D. Muñoz, K. J. Mullinger, T. M. Tierney, and S. Bestmann, *et al.*, Moving magnetoencephalography towards real-world applications with a wearable system, *Nature* **555**, 657 (2018).
- [13] R. Zhang, W. Xiao, Y. Ding, Y. Feng, X. Peng, L. Shen, C. Sun, T. Wu, Y. Wu, Y. Yang, Z. Zheng, X. Zhang, J. Chen, and H. Guo, Recording brain activities in unshielded earth's field with optically pumped atomic magnetometers, *Sci. Adv.* **6**, eaba8792 (2020).
- [14] W. Xiao, C. Sun, L. Shen, Y. Feng, M. Liu, Y. Wu, X. Liu, T. Wu, X. Peng, and H. Guo, A movable unshielded magnetocardiography system, *Sci. Adv.* **9**, eadg1746 (2023).
- [15] I. Kominis, T. Kornack, J. Allred, and M. V. Romalis, A subfemtotesla multichannel atomic magnetometer, *Nature* **422**, 596 (2003).
- [16] H. Dang, A. C. Maloof, and M. V. Romalis, Ultrahigh sensitivity magnetic field and magnetization measurements with an atomic magnetometer, *Appl. Phys. Lett.* **97**, 151110 (2010).
- [17] D. Sheng, S. Li, N. Dural, and M. V. Romalis, Subfemtotesla Scalar Atomic Magnetometry Using Multipass Cells, *Phys. Rev. Lett.* **110**, 160802 (2013).
- [18] B. Shahriari, K. Swersky, Z. Wang, R. P. Adams, and N. de Freitas, Taking the human out of the loop: A review of Bayesian optimization, *Proc. IEEE* **104**, 148 (2016).
- [19] M. R. Bonyadi and Z. Michalewicz, Particle swarm optimization for single objective continuous space problems: A review, *Evol. Comput.* **25**, 1 (2017).
- [20] H.-G. Beyer and H.-P. Schwefel, Evolution strategies—A comprehensive introduction, *Nat. Comput.* **1**, 3 (2002).
- [21] S. Kirkpatrick, C. D. Gelatt, and M. P. Vecchi, Optimization by simulated annealing, *Science* **220**, 671 (1983).
- [22] A. D. Tranter, H. J. Slatyer, M. R. Hush, A. C. Leung, J. L. Everett, K. V. Paul, P. Vernaz-Gris, P. K. Lam, B. C. Buchler, and G. T. Campbell, Multiparameter optimisation of a magneto-optical trap using deep learning, *Nat. Commun.* **9**, 1 (2018).
- [23] E. T. Davletov, V. V. Tsyganok, V. A. Khlebnikov, D. A. Pershin, D. V. Shaykin, and A. V. Akimov, Machine learning for achieving Bose-Einstein condensation of thulium atoms, *Phys. Rev. A* **102**, 011302 (2020).
- [24] A. J. Barker, H. Style, K. Luksch, S. Sunami, D. Garrick, F. Hill, C. J. Foot, and E. Bentine, Applying machine learning optimization methods to the production of a quantum gas, *Mach. Learn.: Sci. Technol.* **1**, 015007 (2020).
- [25] Z. Vendeiro, J. Ramette, A. Rudelis, M. Chong, J. Sinclair, L. Stewart, A. Urvoy, and V. Vuletić, Machine-learning-accelerated Bose-Einstein condensation, *Phys. Rev. Res.* **4**, 043216 (2022).
- [26] E. Zahedinejad, J. Ghosh, and B. C. Sanders, High-Fidelity Single-Shot Toffoli Gate Via Quantum Control, *Phys. Rev. Lett.* **114**, 200502 (2015).
- [27] F. Poggiali, P. Cappellaro, and N. Fabbri, Optimal Control for One-Qubit Quantum Sensing, *Phys. Rev. X* **8**, 021059 (2018).
- [28] M. Bukov, A. G. R. Day, D. Sels, P. Weinberg, A. Polkovnikov, and P. Mehta, Reinforcement Learning in Different Phases of Quantum Control, *Phys. Rev. X* **8**, 031086 (2018).
- [29] P. Rembold, N. Oshnik, M. M. Müller, S. Montangero, T. Calarco, and E. Neu, Introduction to quantum optimal control for quantum sensing with nitrogen-vacancy centers in diamond, *AVS Quantum Sci.* **2**, 024701 (2020).
- [30] V. Dunjko and H. J. Briegel, Machine learning & artificial intelligence in the quantum domain: A review of recent progress, *Rep. Prog. Phys.* **81**, 074001 (2018).
- [31] G. Carleo, I. Cirac, K. Cranmer, L. Daudet, M. Schuld, N. Tishby, L. Vogt-Maranto, and L. Zdeborová, Machine learning and the physical sciences, *Rev. Mod. Phys.* **91**, 045002 (2019).
- [32] S. Ju, T. Shiga, L. Feng, Z. Hou, K. Tsuda, and J. Shiomi, Designing Nanostructures for Phonon Transport via Bayesian Optimization, *Phys. Rev. X* **7**, 021024 (2017).
- [33] S. Ju, Y. Miura, K. Yamamoto, K. Masuda, K.-i. Uchida, and J. Shiomi, Machine learning analysis of tunnel magnetoresistance of magnetic tunnel junctions with disordered MgAl_2O_4 , *Phys. Rev. Res.* **2**, 023187 (2020).
- [34] B. J. Shields, J. Stevens, J. Li, M. Parasram, F. Damani, J. I. M. Alvarado, J. M. Janey, R. P. Adams, and A. G. Doyle, Bayesian reaction optimization as a tool for chemical synthesis, *Nature* **590**, 89 (2021).
- [35] K. Terayama, M. Sumita, R. Tamura, and K. Tsuda, Black-box optimization for automated discovery, *Acc. Chem. Res.* **54**, 1334 (2021).
- [36] J. Kim, D. Kang, S. Kim, and H. W. Jang, Catalyze materials science with machine learning, *ACS Mater. Lett.* **3**, 1151 (2021).
- [37] B. P. Abbott, *et al.*, (LIGO Scientific Collaboration) LIGO: The laser interferometer gravitational-wave observatory, *Rep. Prog. Phys.* **72**, 076901 (2009).
- [38] A. Derevianko and M. Pospelov, Hunting for topological dark matter with atomic clocks, *Nat. Phys.* **10**, 933 (2014).

- [39] J. J. Love and A. Chulliat, An international network of magnetic observatories, *Eos Trans. AGU* **94**, 373 (2013).
- [40] J. Dupont-Roc, S. Haroche, and C. Cohen-Tannoudji, Detection of very weak magnetic fields (10^{-9} gauss) by ^{87}Rb zero-field level crossing resonances, *Phys. Lett. A* **28**, 638 (1969).
- [41] J. Kitching, Chip-scale atomic devices, *Appl. Phys. Lett.* **5**, 031302 (2018).
- [42] V. G. Lucivero, A. Zanoni, G. Corrielli, R. Osellame, and M. W. Mitchell, Laser-written vapor cells for chip-scale atomic sensing and spectroscopy, *Opt. Express* **30**, 27149 (2022).
- [43] O. Alem, T. H. Sander, R. Mhaskar, J. LeBlanc, H. Eswaran, U. Steinhoff, Y. Okada, J. Kitching, L. Trahms, and S. Knappe, Fetal magnetocardiography measurements with an array of microfabricated optically pumped magnetometers, *Phys. Med. Biol.* **60**, 4797 (2015).
- [44] K. Jensen, R. Budvytyte, R. A. Thomas, T. Wang, A. M. Fuchs, M. V. Balabas, G. Vasilakis, L. D. Mosgaard, H. C. Stärkind, and J. H. Müller, *et al.*, Non-invasive detection of animal nerve impulses with an atomic magnetometer operating near quantum limited sensitivity, *Sci. Rep.* **6**, 29638 (2016).
- [45] A. Borna, T. R. Carter, J. D. Goldberg, A. P. Colombo, Y.-Y. Jau, C. Berry, J. McKay, J. Stephen, M. Weisend, and P. D. D. Schwindt, A 20-channel magnetoencephalography system based on optically pumped magnetometers, *Phys. Med. Biol.* **62**, 8909 (2017).
- [46] S. P. Krzyzewski, A. R. Perry, V. Gerginov, and S. Knappe, Characterization of noise sources in a microfabricated single-beam zero-field optically-pumped magnetometer, *J. Appl. Phys.* **126**, 044504 (2019).
- [47] M. E. Limes, E. L. Foley, T. W. Kornack, S. Caliga, S. McBride, A. Braun, W. Lee, V. G. Lucivero, and M. V. Romalis, Portable Magnetometry for Detection of Biomagnetism in Ambient Environments, *Phys. Rev. Appl.* **14**, 011002 (2020).
- [48] M. N. Nabighian, V. Grauch, R. Hansen, T. LaFehr, Y. Li, J. W. Peirce, J. D. Phillips, and M. Ruder, The historical development of the magnetic method in exploration, *Geophysics* **70**, 33ND (2005).
- [49] R. Parker, A. Ruffell, D. Hughes, and J. Pringle, Geophysics and the search of freshwater bodies: A review, *Sci. Justice* **50**, 141 (2010).
- [50] W. E. Bell and A. L. Bloom, Optically Driven Spin Precession, *Phys. Rev. Lett.* **6**, 280 (1961).
- [51] Z. D. Grujić and A. Weis, Atomic magnetic resonance induced by amplitude-, frequency-, or polarization-modulated light, *Phys. Rev. A* **88**, 012508 (2013).
- [52] B. Patton, E. Zhivun, D. C. Hovde, and D. Budker, All-Optical Vector Atomic Magnetometer, *Phys. Rev. Lett.* **113**, 013001 (2014).
- [53] M. Petrenko, A. Pazgalev, and A. Vershovskii, Single-Beam All-Optical Nonzero-Field Magnetometric Sensor for Magnetoencephalography Applications, *Phys. Rev. Appl.* **15**, 064072 (2021).
- [54] V. Lebedev, S. Hartwig, and T. Middelmann, Fast and robust optically pumped cesium magnetometer, *Adv. Opt. Technol.* **9**, 275 (2020).
- [55] R. Li, F. N. Baynes, A. N. Luiten, and C. Perrella, Continuous High-Sensitivity and High-Bandwidth Atomic Magnetometer, *Phys. Rev. Appl.* **14**, 064067 (2020).
- [56] N. Wilson, C. Perrella, R. Anderson, A. Luiten, and P. Light, Wide-bandwidth atomic magnetometry via instantaneous-phase retrieval, *Phys. Rev. Res.* **2**, 013213 (2020).
- [57] T. Bryś, S. Czekaj, M. Daum, P. Fierlinger, D. George, R. Henneck, M. Kasprzak, K. Kirch, M. Kuźniak, G. Kuehne, A. Pichlmaier, A. Siodmok, A. Szalc, L. Tanner, C. Assmann, S. Bechstein, D. Drung, T. Schurig, C. Ciofi, and B. Neri, Magnetic field stabilization for magnetically shielded volumes by external field coils, *Nucl. Instrum. Meth. A* **554**, 527 (2005).
- [58] G. O. Forte, G. Farrher, L. R. Canali, and E. Ansaldo, Automatic shielding-shimming magnetic field compensator for excluded volume applications, *IEEE Trans. Control Syst. Technol.* **18**, 976 (2010).
- [59] N. Holmes, T. M. Tierney, J. Leggett, E. Boto, S. Mellow, G. Roberts, R. M. Hill, V. Shah, G. R. Barnes, and M. J. Brookes, *et al.*, Balanced, bi-planar magnetic field and field gradient coils for field compensation in wearable magnetoencephalography, *Sci. Rep.* **9**, 14196 (2019).
- [60] R. Zhang, Y. Ding, Y. Yang, Z. Zheng, J. Chen, X. Peng, T. Wu, and H. Guo, Active magnetic-field stabilization with atomic magnetometer, *Sensors* **20**, 4241 (2020).
- [61] K.-M. C. Fu, G. Z. Iwata, A. Wickenbrock, and D. Budker, Sensitive magnetometry in challenging environments, *AVS Quantum Sci.* **2**, 044702 (2020).
- [62] G. Bevilacqua, V. Biancalana, Y. Dancheva, and A. Vigiante, Self-Adaptive Loop for External-Disturbance Reduction in a Differential Measurement Setup, *Phys. Rev. Appl.* **11**, 014029 (2019).
- [63] Z.-M. Zhai, M. Moradi, L.-W. Kong, and Y.-C. Lai, Detecting Weak Physical Signal from Noise: A Machine-Learning Approach with Applications to Magnetic-Anomaly-Guided Navigation, *Phys. Rev. Appl.* **19**, 034030 (2023).
- [64] R. Zhang, B. Pang, W. Li, Y. Yang, J. Chen, X. Peng, and H. Guo, in *2018 IEEE International Frequency Control Symposium (IFCS)* (IEEE, Olympic Valley, CA, USA, 2018), p. 1.
- [65] D. Sheng, A. R. Perry, S. P. Krzyzewski, S. Geller, J. Kitching, and S. Knappe, A microfabricated optically-pumped magnetic gradiometer, *Appl. Phys. Lett.* **110**, 031106 (2017).
- [66] B. Selman, H. A. Kautz, and B. Cohen, in *Proceedings of the Twelfth AAAI National Conference on Artificial Intelligence, AAAI-94* (AAAI Press, Seattle, Washington, 1994), p. 337.